Direct Numerical Simulation of Noise and its Source from Decaying Homogeneous Isotropic Turbulence with Particulates

Wei Wang and Steven A. E. Miller

University of Florida, Department of Mechanical and Aerospace Engineering, Gainesville, Florida, 32611, United States. Email: saem@ufl.edu

Abstract

Eulerian-Lagrangian direct numerical simulations of the compressible Navier-Stokes equations are performed for decaying homogeneous isotropic turbulence. Particles are suspended within the turbulent field. A parametric study of over fifty simulations is performed that varies the number of particles and their diameter. The Crighton Ffowcs Williams acoustic analogy is used to predict the noise from the turbulent field with suspended particles. The traditional quadrupole source of Lighthill dominates the radiated noise for low particle number or diameter. As the number of particles or their diameter increase, the root-mean-square pressure scales as the five-halves power of the volume fraction, which indicates that noise is dominated by the monopole and dipole terms.

Keywords: direct numerical simulation, multiphase, particle, acoustic analogy, noise

1. Introduction

The noise from rockets is harmful to the surrounding environment, community, and causes vibroacoustic response on the rocket fuselage [1]. A major portion of this noise is due to the turbulent rocket exhaust that is filled with solid propellant combustion products. There are many numerical investigations of the noise from solid rocket boosters [2, 3, 4], where the flow-particles coupling in the exhaust alter or increase the noise. However, very little research attention has been given to the study of the fundamental source of noise from particle-laden turbulence in a fundamental flow. We must understand the fundamental mechanisms of noise generation by particles in turbulence before we will be able to improve noise source modeling of rocket exhaust noise. For this purpose, we seek to numerically predict the fundamental scaling laws of the acoustic pressure from decaying homogeneous isotopic turbulence. We seek to understand how the number and diameter of particles alter noise in the far-field. We perform parametric studies to quantify the effect of particle density, diameter, and mass loading on the far-field noise generated by a homogeneous isotropic turbulent suspension. This is performed with a direct numerical simulation (DNS) solver for the compressible Navier-Stokes equations with a Lagrangian particle dynamics solver.

We are studying particle laden homogeneous turbulence due to its wide presence in industrial flows, and to understand the associated harmful effects of acoustic radiation.

Theory of homogeneous turbulence [5] is well developed and found within many industrial turbulent flows. In fact, turbulence has a natural tendency to return to isotropy (see Lumley and Newman [6]). Many particle laden flows contain regions of homogeneous isotropic turbulence, and can be found in rotating turbulent flows [7], within internal waves [8], rocket exhaust [2, 3, 4], and chemically reacting flows [9]. In particular, jet exhaust from rockets contain regions of locally homogeneous turbulence that have returned to isotropy [6]. This local homogeneous turbulence, which contains particulates, radiates as fine-scale mixing noise. The fine-scale mixing noise (see Patel and Miller [10]) is one of the major and dominant components in high-speed jet or rocket noise. One of the purposes of this paper is to understand how the source changes with variation of particles from the solid rocket fuel.

In this study, we vary the number of particulates, turbulence statistics, particle mass, and particle diameter to understand how noise is radiated from fine-scale mixing noise from rocket exhaust. Simulations are extremely expensive, especially when tracking each particle, which can easily overwhelm the most powerful supercomputers today and likely through the authors' lifetime. Therefore, we try and match our simulations as closely as possible with respect to particle size and mass with the experimental measurements of acoustic radiation from rockets of Panda and Mosher [11] and Horne et al. [12].

1.1. Previous Research and Relation to the Present

Squire and Eaton [13] used DNS to study particle response and the modification of turbulence in a stationary homogeneous isotropic flow. They found that light and heavy particles modify the turbulent field differently, because light particles collect preferentially in regions of low vorticity and high strain rate. Boivin et al. [14] investigated stationary isotopic turbulence in a dilute flow. They found that the kinetic energy is dissipated with increasing mass loading, while the effect of the particle response time is not significant. They also confirmed the finding of Squire and Eaton [13], that the distortion of the turbulent kinetic energy (TKE) spectra is not uniform, and it significantly changes the transport of the dissipation rate. In contrast to Squire and Eaton, Elghobashi and Truesdell [15] chose to examine the modification of turbulence by particles in a decaying isotropic field. They focused their study on small particles whose diameter are less than the Kolmogorov length scale of the flow. Their findings agreed with Squire and Eaton [13], in that the particles increase the fluid turbulent energy at high wavenumbers, viscous dissipation rate, and the rate of energy transfer from the large-scale turbulence. Ferrante and Elghobashi [16] used DNS to examine decaying isotropic turbulence, where the particle volume fraction and mass loading were fixed at 10^{-3} and 1, respectively. Their results showed that the particles attenuate the turbulence at small wavenumbers and enhance the turbulence at large wavenumbers compared to particle-free flow.

None of these important and fundamental studies examine how the presence of particles alter radiated noise or change the sound source. Here, we seek to understand how the introduction of particles alters the statistics of homogeneous isotropic decaying turbulence, but more importantly, alters the radiated noise and associated statistics.

Next, we describe the numerical method that integrates the Navier-Stokes equations with Lagrangian particles. This method is used to perform a DNS study for decaying isotropic homogeneous turbulence. The presented results are focused on acoustic calculations of root mean square pressure.

2. Methodology

2.1. Governing Equations

We model the multiphase flow using the filtered Navier-Stokes equations with additional source terms for particulates. The equations are written in integral-vector form as

$$\frac{\partial}{\partial t}\int_{\Omega} \boldsymbol{W} d\Omega + \oint_{\partial\Omega} \boldsymbol{F_c} dS = \oint_{\partial\Omega} \boldsymbol{F_v} dS + \int_{\Omega} \boldsymbol{Q} d\Omega, \tag{1}$$

where $\boldsymbol{F}_c$ is a vector of convective fluxes, $\boldsymbol{F}_v$ is a vector of viscous fluxes, $\boldsymbol{Q}$ is a vector of source terms, t is time, $\boldsymbol{W}$ is a vector of conservative variables, Ω represents volumetric integration, and $\partial\Omega$ represents a flux integral. The vectors $\boldsymbol{W}$, $\boldsymbol{F}_c$, and $\boldsymbol{F}_v$ are

$$\boldsymbol{W} = \left[\rho, \rho u, \rho v, \rho w, \rho E\right]^{\mathsf{T}}, \tag{2}$$

$$\boldsymbol{F_c} = \left[\rho V_n, \rho u V_n + n_x p, \rho v V_n + n_y p, \rho w V_n + n_z p, \rho H V_n\right]^{\mathsf{T}}, \tag{3}$$

and

$$\boldsymbol{F_v} = \begin{bmatrix} 0 \\ n_x\tau_{xx} + n_y\tau_{xy} + n_z\tau_{xz} \\ n_x\tau_{yx} + n_y\tau_{yy} + n_z\tau_{yz} \\ n_x\tau_{zx} + n_y\tau_{zy} + n_z\tau_{zz} \\ n_x\Theta_x + n_y\Theta_y + n_z\Theta_z \end{bmatrix}. \tag{4}$$

Here, E is total energy, H is total enthalpy, and the face normal velocity is $V_n = n_x u + n_y v + n_z w$, where $\boldsymbol{n} = [n_x, n_y, n_z]^{\mathsf{T}}$ is the face normal vector. The shear stress tensor is defined as $\tau_{ij} = 2\mu S_{ij} - (2/3)\mu(\partial v_k/\partial x_k)\delta_{ij}$, where S_{ij} is the strain-rate tensor and μ is dynamic viscosity. Dynamic viscosity is computed from Sutherland's law [17], $\mu = \mu_{ref}(TT_{ref}^{-1})^{3/2}(T_{ref} + S)(T + S)^{-1}$, where $\mu_{ref} = 1.716 \times 10^{-5}$ kgm^{-1}s^{-1}, $T_{ref} = 273.15$ K, $S = 110.4$ K, and δ_{ij} is the Kronecker delta function. The vector $\boldsymbol{\Theta}$ is

$$\Theta_x = u\tau_{xx} + v\tau_{xy} + w\tau_{xz} + k\frac{\partial T}{\partial x}, \tag{5}$$

$$\Theta_y = u\tau_{yx} + v\tau_{yy} + w\tau_{yz} + k\frac{\partial T}{\partial y}, \tag{6}$$

and

$$\Theta_z = u\tau_{zx} + v\tau_{zy} + w\tau_{zz} + k\frac{\partial T}{\partial z}, \tag{7}$$

where k is the thermal conductivity and T is the temperature. Finally, the vector $\boldsymbol{Q}$ is

$$\boldsymbol{Q} = \left[m_p, \rho f_{e,x} + f_{p,x}, \rho f_{e,y} + f_{p,y}, \rho f_{e,z} + f_{p,z}, \dot{q}_h + E_p\right]^{\mathsf{T}}, \tag{8}$$

where E_p is the energy source from particles, $f_{e,i}$ are external volumetric forces, $f_{p,i}$ are momentum sources from particles, m_p is the mass source of particles, and $\dot{q}_h$ is the external heat source. The vector $\boldsymbol{Q}$ represents additional body forces and forces due to the particulates within the flow. Pressure, temperature, and density are related through the ideal gas law, $p = \rho RT$, where R is the gas constant.

2.2. Lagrangian Particles

The evolution equations for position and velocity of a single Lagrangian particle are $\frac{d}{dt}\boldsymbol{x_p} = \boldsymbol{V_p}$ and $m_p \frac{d\boldsymbol{V}_{p,j}}{dt} = \boldsymbol{F}_j$, where $\boldsymbol{x_p} = \left[x_p, y_p, z_p\right]^\mathsf{T}$ is the position vector of the particle, $\boldsymbol{V_p}$ is the velocity vector of the particle, and $\boldsymbol{F}_j$ is the total force acting on the j^{th} particle. The total force acting on a single particle can be further decomposed into an aerodynamic force and a force due to particle-particle collision. Particle collisions are very rare, therefore are neglected [18].

Aerodynamic force, $\boldsymbol{F}$, is the force that a single particle exerts on the gas [19, 20, 21, 22, 18]

$$\boldsymbol{F} = \boldsymbol{F}_{pg} + \boldsymbol{F}_{qs} + \boldsymbol{F}_{iu} + \boldsymbol{F}_{vu}, \tag{9}$$

where $\boldsymbol{F}_{pg}$, $\boldsymbol{F}_{qs}$, $\boldsymbol{F}_{iu}$, and $\boldsymbol{F}_{vu}$ are pressure gradient, quasi-steady, inviscid unsteady, and viscous unsteady force, respectively.

The pressure gradient force is the undisturbed force [22]. The volume occupied by the particle experiences the pressure gradient force no matter whether the particle exists or not. In other words, the gas phase occupying the same volume would experience the same force in a single phase flow. The other three forces only occur due to the presence of the particle that occupies a volume of gas, or in other words, disturbed the flow. The pressure gradient force is calculated by

$$\boldsymbol{F}_{pg} = \frac{3}{4}\pi R_p^3 \rho \frac{D\boldsymbol{V}}{Dt}, \tag{10}$$

where $\frac{D\boldsymbol{V}}{Dt}$ is the acceleration of the gas. Here, $\frac{D}{Dt}$ denotes the material derivative.

The quasi-steady force is often recognized as Stokes' drag in steady uniform flow[22]. Although both the particle and gas around it experience strong unsteadiness, Stokes' drag is represented in a quasi-steady sense using the instantaneous relative velocity between particle and ambient flow. We define the Stokes' drag as

$$\boldsymbol{F}_{qs} = 6\pi\mu_f R_p(\boldsymbol{V} - \boldsymbol{V}_p). \tag{11}$$

The inviscid unsteady and the viscous unsteady flow arise due to the relative acceleration between the particle and ambient flow[22]. The inviscid unsteady force, or added-mass force, is

$$\boldsymbol{F}_{iu} = -\frac{1}{2} m_f \left(\frac{d\boldsymbol{V}_p}{dt} - \frac{d\boldsymbol{V}}{dt}\right). \tag{12}$$

This force is due to the no-penetration boundary condition of the disturbed flow. As a result, gas around the particle are accelerated with it. The mass of the gas is the added-mass. Thus, additional force needs to be applied to the particle to increase the kinetic energy of the added-mass of gas that accelerates with the particle.

The viscous unsteady force, or the Basset history force, represents the viscous effect associated with relative acceleration of the particle and ambient flow[22]. It arises because of the no-slip boundary condition on the particle surface. The viscous unsteady force takes the form of

$$\boldsymbol{F}_{vu} = 6R_p^2\rho\sqrt{\pi\nu}\int_{-\infty}^{t} K_{vu}(t-\xi)\left[\frac{d\boldsymbol{V}}{dt} - \frac{d\boldsymbol{V}_p}{dt}\right]_{\xi} d\xi, \tag{13}$$

where $K_{vu}(t) = t^{-1/2}$ is Basset history kernel and $[\quad]_{\xi}$ denotes the value inside the bracket is to be evaluated at time ξ. The equation for the particle's temperature is $\frac{d}{dt}T_p = \frac{T-T_p}{\tau^{\theta}}$, where T and T_p are the temperature of the gas phase at the particle position and the temperature of the particle, respectively. The particle response and thermal response times[18] are modeled as

$$\tau^{u} = \frac{\rho_p d_p^2}{18\mu f_u(Re_p)} \tag{14}$$

and

$$\tau^{\theta} = \frac{c_{p,p}\rho_p d_p^2}{12k f_{\theta}(Re_p)}, \tag{15}$$

where $c_{p,p}$ is the specific heat of the particle, d_p is the diameter of the particle, ρ_p is the density of the particle, and μ is the dynamic viscosity of the gas phase evaluated at the particle position. Since Re_p is typically larger than unity, we use the following correlation of Naumann [23] for Stokes' drag $f_u(Re_p) = 1 + 0.15Re_p^{0.687}$, and the Ranz-Marshall correlation [24] for energy $f_{\theta}(Re_p) = 1 + 0.3Re_p^{1/2}Pr^{1/3}$. The particle Reynolds number is

$$Re_p = \frac{d_p|\boldsymbol{V} - \boldsymbol{V}_p|}{\nu}. \tag{16}$$

Here, ν is the kinematic viscosity of gas at the particle position. Forces exerted by particles on the fluid are

$$\boldsymbol{f}_p = -\sum \frac{\pi d_p^3\rho_p}{6\tau^{u}}(\boldsymbol{V_p} - \boldsymbol{V}), \tag{17}$$

where $\sum$ denotes summation over all the particles within the finite volume cell. Energy transfer from each individual particle to the surrounding fluid is governed by

$$E_p = \sum\left[\boldsymbol{f}_p \cdot \left(\boldsymbol{V}_p - \boldsymbol{V}\right) - \frac{\pi d_p^3\rho_p c_{p,p}}{6\tau^{\theta}}(T_p - T)\right]. \tag{18}$$

2.3. Numerical Method

The numerical code used for aerodynamic calculations is RocfluidMP. It was originally developed by the Center for Simulation of Advanced Rockets at the University of Illinois at Urbana-Champaign and extended at the Center for Compressible Multiphase Turbulence at the University of Florida. This code has been extensively used to simulate multiphase flow within rockets, jets, and plumes [25, 26, 27].

2.3.1. Discretization scheme

RocfluidMP is an unstructured second order accurate finite volume compressible Navier-Stokes code with a number of models for multi-physics coupling. In this study, the multi-physics model RocPart, which handles computations of the Lagrangian particles, is also used. As an unstructured Navier-Stokes solver, cell stencils are needed for discretizing the interpolation and gradient operators. The flow solution at each cell face is reconstructed using the weighted essentially non-oscillatory (WENO) scheme. The details of the WENO scheme used here is shown in Haselbacher [28].

2.3.2. Time Integration

Both the gas phase and the disperse phase are advanced in time numerically. We choose to use the 3^{rd} order explicit Runge-Kutta(RK) scheme developed by Wray [29] because of its high efficiency and low memory use. Because more equations are involved in multiphase simulations relative to single-phase simulations, the memory efficiency of the RK scheme is essential. Wray's [29] 3^{rd} order RK scheme only require 2 registers of memory, which is much less than the 4 registers of the traditional RK4 scheme.

2.3.3. Lagrangian Particle Tracking

We use a robust trajectory based particle-localization algorithm [30] to find the destination cell of a particle at each time step. At each time step, we know the initial location and velocity of each particle. For example the particle is in the cell C_1. Then we determine which cell face of C_1 the particle's trajectory intersect and particle must move to the cell C_2 that is adjacent to the intersection face. We apply this process repeatedly until the particle moves to its destination along the trajectory, we can determine the cell C_n at the end of current time step and use C_n as the starting position for the next time step. Haselbacher et al. [30] describe the algorithm in more detail and evaluate the efficiency on an unstructured grid.

To evaluate gas properties at the particle locations for Eqn. (17) and (18), we used a 2nd-order accurate piece-wise linear interpolation. Assume the particle is located in cell i. The gas properties ϕ_g at particle location $\boldsymbol{x}_p$ are calculated as

$$\phi_p(\boldsymbol{x}_p) = \phi_i + (\boldsymbol{\delta\phi})_i \cdot (\boldsymbol{x}_p - \boldsymbol{x}_i), \tag{19}$$

where ϕ_i is the gas properties at the cell center, $\boldsymbol{x}_i$ is the cell centroid location, and $\boldsymbol{\delta\phi}$ is the discrete gradient of ϕ calculated using the WENO scheme [28].

2.3.4. Eulerian-Lagrangian Interaction

The particles affect the momentum and energy of the gas phase through the source terms given in Eqn. (8). Sources from all particles within a cell contribute to the cell only. Equations (17) and (18) are evaluated at each time step for all the particles inside a cell. Then the source is coupled into the cell's momentum and energy transport. In this way, the particle and gas phase are two-way coupled.

2.3.5. Crighton and Ffowcs Williams' Acoustic Analogy for Two-Phase Flow

We implemented Crighton and Ffowcs Williams's acoustic analogy [31] into the RocfluidMP solver as a sub-model for the particle-laden flow simulations. The C-FW acoustic analogy is

$$\left(\frac{1}{c_\infty^2}\frac{\partial^2}{\partial t^2}+\nabla^2\right)p' = \frac{\partial Q}{\partial t} - \frac{\partial G_i}{\partial x_i} + \frac{\partial^2 T_{ij}}{\partial x_i x_j}, \tag{20}$$

where $\frac{\partial Q}{\partial t}$, $-\frac{\partial G_i}{\partial x_i}$, and $\frac{\partial^2 T_{ij}}{\partial x_i x_j}$ are the source terms that need to be evaluated using the flow-field from the CFD solver. p' is the acoustic pressure outside the turbulent field. We choose to solve Eqn. (20) analytically in the time domain. The analytical solution of Eqn. (20) are derived using the free-space Green's function $g(\boldsymbol{x}, t, \boldsymbol{y}, \tau)$ that satisfies

$$\left(\frac{1}{c_\infty^2}\frac{\partial^2}{\partial t^2}+\nabla^2\right)g(\boldsymbol{x}, t, \boldsymbol{y}, \tau) = \delta(\boldsymbol{x}-\boldsymbol{y})\delta(t-\tau). \tag{21}$$

The solution in the far-field is in the form of convolution of $g(\boldsymbol{x}, t, \boldsymbol{y}, \tau)$ and the source terms, $\frac{\partial Q}{\partial t} - \frac{\partial G_i}{\partial x_i} + \frac{\partial^2 T_{ij}}{\partial x_i x_j}$, more specifically

$$\begin{aligned} 4\pi p'(\boldsymbol{x}, t) = &\frac{1}{|\boldsymbol{x}|}\int \frac{\partial}{\partial t} Q\left(\boldsymbol{y}, t - \frac{|\boldsymbol{x}-\boldsymbol{y}|}{c_\infty}\right) dy \\ &- \frac{x_i}{|\boldsymbol{x}|^2}\frac{1}{c_\infty}\int \frac{\partial}{\partial t} G_i\left(\boldsymbol{y}, t - \frac{|\boldsymbol{x}-\boldsymbol{y}|}{c_\infty}\right) dy \\ &+ \frac{x_i x_j}{|\boldsymbol{x}|^3}\frac{1}{c_\infty^2}\int \frac{\partial^2}{\partial t^2} T_{ij}\left(\boldsymbol{y}, t - \frac{|\boldsymbol{x}-\boldsymbol{y}|}{c_\infty}\right) dy. \end{aligned} \tag{22}$$

Since neither the observer nor the computational grid move, we implemented the retarded time algorithm to compute far-field acoustic pressure. The retarded-time algorithm is very efficient and easy to parallelize [32], therefore, we were able to run the acoustic calculation within the CFD solver with little overhead. Equation (22) is approximated as follows

$$\begin{aligned} 4\pi p'(\boldsymbol{x}, t) \approx &\sum \frac{1}{|\boldsymbol{x}|}\frac{\partial}{\partial t} Q_l(\tau_l) V_l - \sum \frac{x_i}{|\boldsymbol{x}|^2}\frac{1}{c_\infty}\frac{\partial}{\partial t} G_{l,i}(\tau_l) V_l \\ &+ \sum \frac{x_i x_j}{|\boldsymbol{x}|^3}\frac{1}{c_\infty^2}\frac{\partial^2}{\partial t^2} T_{l,ij}(\tau_l) V_l, \end{aligned} \tag{23}$$

where subscription l denote the cell-center value of l^{th} cells, $\tau_l = t - \frac{|\boldsymbol{x}-\boldsymbol{y}_l|}{c_\infty}$ is the retarded-time evaluated using at the cell center $\boldsymbol{y}_l$, V_l is the cell volume, and the summation is over all the cells.

The time history of acoustic pressure at the observer can be found by determining the observer time and evaluating the summation in Eqn. (23). The retarded-time, τ_l, for all cells is determined solely based on the observer time the cells' location, because observer is stationary. Linear interpolation in time is used for evaluating the source strength at the retarded-time. Since the retarded-time varies for each cell, a short time history of source strength is stored and updated at each CFD time step.

2.3.6. Equations of Initial Conditions

The domain's boundary conditions are set to be periodic in the x, y, and z directions. The three dimensional initial velocity field at $t = 0$ is generated to follow composite energy spectrum presented by Schumann and Patterson [33]

$$E(k,0) = \left(\frac{1}{2\pi}\right)\left(\frac{3}{2}u_0^{*2}\right)\left(\frac{k}{k_p^2}\right)\exp\left(-\frac{k}{k_p}\right). \tag{24}$$

where u_0^* is the initial root-mean-square (rms) velocity, k is the wavenumber, and k_p is the wavenumber at peak energy. Figure 1 shows the non-dimensional initial energy spectrum $E(k,0)$ with respect to the wavenumber k/k_{min}, and the spectrum is normalized with $< u^2 >= 2/3 \int_0^\infty E(k,0)dk$.

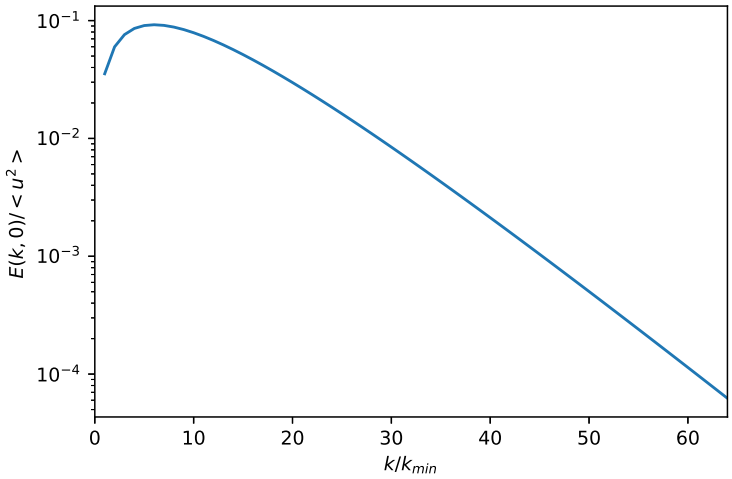

Figure 1: Initial TKE, $E(k,0)$, for $k_p k_{min}^{-1} = 6$.

This energy spectrum is shown to be more suitable for simulations of decaying homogeneous and isotropic turbulence, since the decay rate of the turbulent energy during the initial period matches power law of decay TKE $\propto (t-t_0)^{-1}$, where t_0 is the virtual starting time of decay. We adopt the initialization procedure of Krianchnan [34]. The initialization algorithm ensures the generated initial velocity field is divergence-free, isotropic, periodic in three directions, and the prescribed energy spectrum is obtained.

The integral length scale l_0, Taylor microscale λ_0, Kolmogorov length scale η_0, Reynolds number based on the initial Taylor microscale Re_{λ_0}, and the dissipation rate ϵ_0 are given as

$$l_0 = \frac{1}{2u_0^2}\int_0^\infty \frac{E(k,0)}{k}dk, \tag{25}$$

$$\lambda_0 = \left(\frac{15\nu u_0^2}{\epsilon_0}\right)^{1/2}, \tag{26}$$

$$\eta_0 = \left(\frac{\nu^3}{\epsilon}\right)^{1/4}, \tag{27}$$

$$Re_{\lambda_0} = \frac{u_0 \lambda_0}{\nu}, \tag{28}$$

and

$$\epsilon_0 = 2\nu \int_0^\infty k^2 E(k,0) dk. \tag{29}$$

3. Results

The particles suspended in a turbulent flow generate noise through the coupling with the fluid phase. We seek to understand what parameters of the particles alter the noise in the far-field, and to what extent each of the parameters alter the noise source. We perform parametric studies to quantify the effect of particle density, diameter, and mass loading on the far-field noise generated by a homogeneous isotropic turbulent suspension.

3.0.1. Initial Conditions

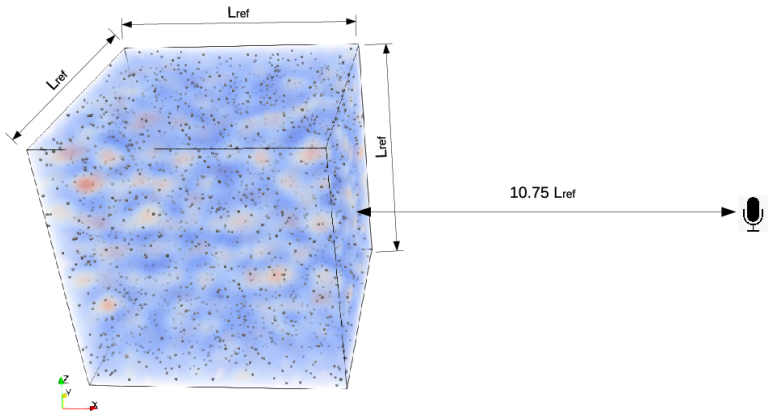

Figure 2: Schematic sketch.

We initialize mono-disperse particles at random locations within a cubic computational domain. We focus on varying the number of particles and their diameter within the turbulent field to understand the effect on noise radiation. Table 1 shows the physical parameters of the suspended particles. Figure 2 shows the sketch of the case setup. The flow-field is resolved in a cubic flow domain of width L_{ref} = 0.1859 m and grid resolution of 262,144 (64^3) points. Here, L_{ref} is the reference length scale and the length of each side of the computational domain. The wavenumbers in Eqn. (24) are normalized by k_{min}, which is 33.8 rad per meter. The total number of particles varies from 10^3 to 10^5, and the particle diameters vary from 10 μ m to 200 μ m. Two sets of 25 simulations (50 total) corresponding to each combination of the particle diameter and total particle numbers in Table 1 are simulated for initial gas velocity fields of u_{rms} = 0.0504 m/s and u_{rms} = 0.2016

Table 1: Physical parameters for the suspension of particles.

Parameters					
Particle number (thousands)	1	5	10	50	100
Particle diameter (10^{-6} m)	10	50	100	150	200

m/s, respectively. The particles are injected within the flow-field at random locations, and the particle initial velocities are equal to the local fluid velocity.

A number of important parameters for particle laden flow are defined to help understand the simulations. The volume fraction of the particles is $\alpha = \delta V_p \delta V^{-1}$, where δV_p is the volume of the particles in the volume of mixture δV. The particle mass loading is defined as $\phi = \alpha \rho_p \rho_f^{-1}$, where ρ_p and ρ_f are the densities of the particles and the fluid. The particles response time to the surrounding fluid is $\tau_p = \rho_p d_p^2 (18 \rho_f \nu)^{-1}$. The Kolmogorov time scale of the carrier phase is $\tau_k = \eta^2 \nu^{-1}$. The Stokes number is defined as the ratio of the particle response time and the Kolmogorov time scale as $\mathrm{St} = \tau_p \tau_k^{-1}$. Finally, the Reynolds number of a particle is defined as $\mathrm{Re}_p = |u_p - u_f| d_p \nu^{-1}$.

Figure 3 shows the temporal development of the integral scale, l, Taylor microscale, and the Kolmogorov length scale for the base case in which particles are not present. This case is important because it represents the simulation where no noise from particulates are present. All the time scales increase moderately as the simulation advances, and the integral, Taylor, and the Kolmogorov scales reach 0.024 m, 0.013 m, and 0.0025 m, respectively at $t^* = 10.3$.

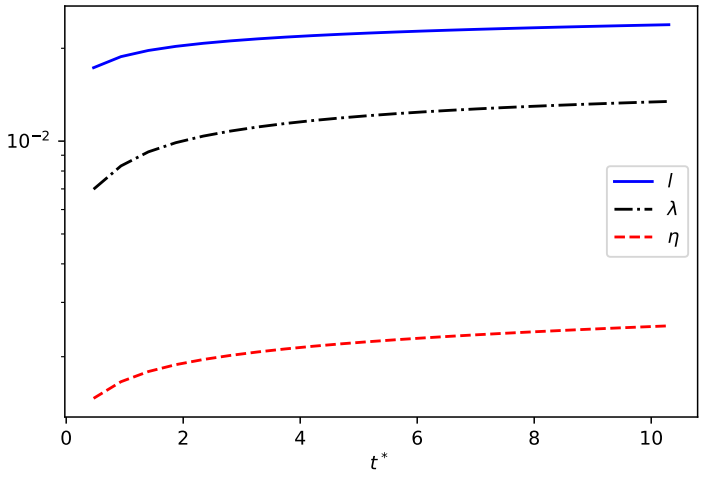

Figure 3: Variation of l, λ, and η with simulation time for the base DNS case without particles.

Figure 4 shows the decay of the RMS fluid velocity, u_{rms}, which is calculated as $u_{rms} = (2/3 \int_0^\infty E(k)dk)^{1/2}$ and is normalized with $u_{rms,0}$ at $t^* = 0$. u_{rms} decays as expected to approximately 65% at $t^* = 10.3$. The Reynolds numbers based on the integral scale and Taylor microscale are initially around 28 and 15, and decay to 14 and 7, respectively.

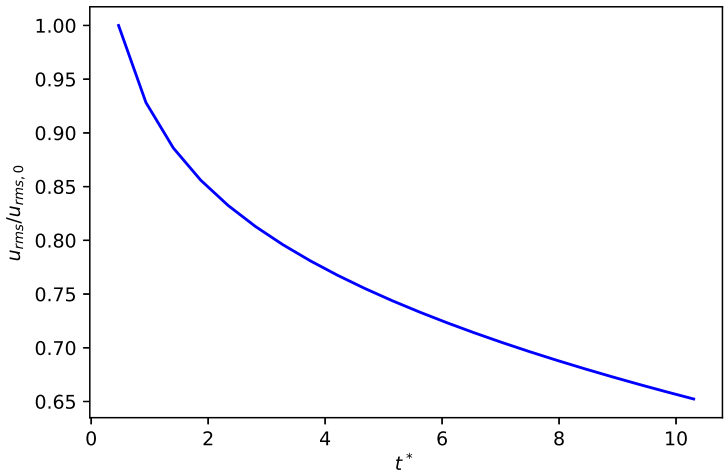

Figure 4: Time development of u_{rms}.

The spatial resolution for the smallest turbulent motion is estimated by the dimensionless number ηk_{max}, and k_{max} is the highest estimated resolved wavenumber $\frac{2\pi}{L}(\frac{N}{2})$. Figure 5 shows the variation of ηk_{max}, and ηk_{max} is greater than 1.5 for $t^* > 0.5$, which indicates the scale is resolved.

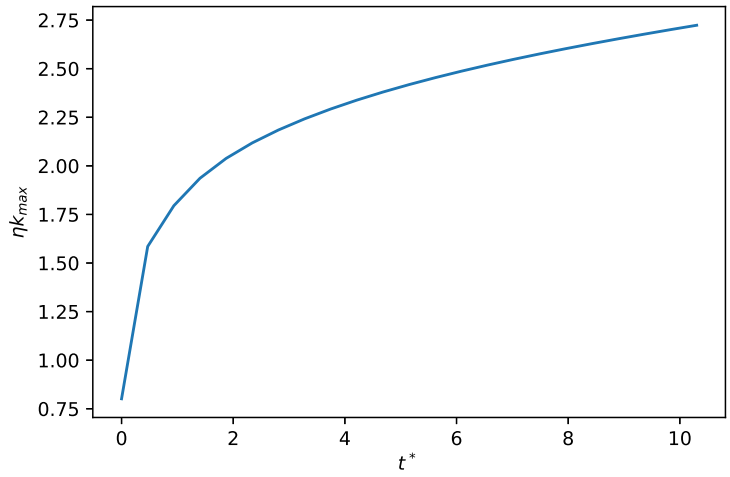

Figure 5: Spatial resolution of the Kolmogorov scale and temporal development of ηk_{max}.

The trends of decay for the low Reynolds number particle free cases as shown in Figs. 3 through 5 match those of traditional studies. For example, the single phase study of Sarkar and Hussaini [35] matches decay rate of u_{rms} and the growth of l, λ, and η. Similar trends are reported in [36, 37, 38].

Figure 6 shows the time development of the energy spectra of the flow versus the magnitude of the wavenumber vector, $|k|$. The spectra at any time t is calculated by integrating the Fourier transform of the trace of the velocity correlation tensor over the spherical shell of radius k. Spectra at different times t^* are normalized with $\int_0^\infty E(k,t)dk$. A line representing Kolmogorov's -5/3 law is fitted within Fig. 6.

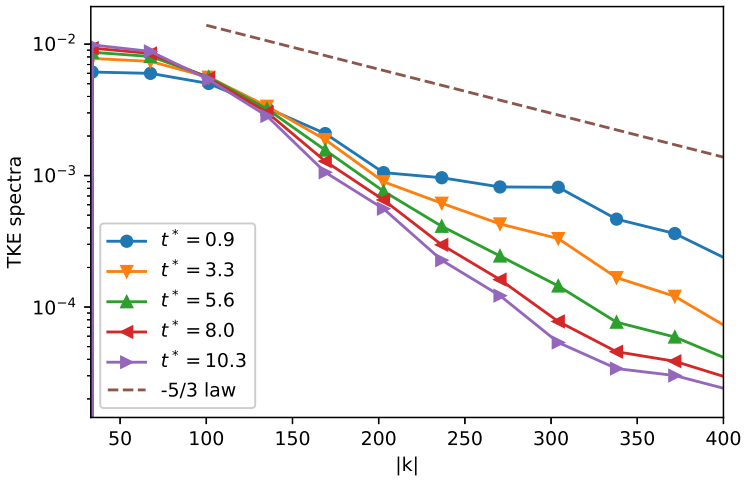

Figure 6: Temporal variation of $E(k, t^*)$ versus $|k|$.

Figures 7 and 8 show the variation of the RMS far-field acoustic pressure changes with respect to the change of total number of particles inside the domain and the diameter of all particles (see Table 1). The observer is located 10.75 L_{ref} away from the center of the domain. Figure 7 corresponds to cases with initial fluid velocity u_{rms} = 0.0504 m/s, it shows u_{rms} = 0.2016 m/s at t^* = 0. p_{rms} is calculated from the pressure time history, $p_{rms} = \left(1/T \int_0^T p'^2(t)dt\right)^{1/2}$. Here, T = 0.013 s is chosen such that the p' fluctuation for all cases are orders of magnitude lower than the initial pressure fluctuation, hence the vast majority of total acoustic energy is included.

We found no change in directivity at any frequency within our acoustic predictions. This is expected because of the invariant nature of the turbulent statistics in isotropic flow-fields. Single phase simulations, such as those of Sarkar and Hussaini [35], also show no major directivity. Extremely sparse particle fields with large particle diameters would likely present some directivity in the acoustic field.

In general, p_{rms} increases with increasing number of particles and increasing particle diameter. However, the effect of the number of particles and their diameters are not independent of each other. Figure 7(a) shows that a small number of particles do not strongly impact the far-field noise level in the cases of smaller particles (diameters less than 10^{-4} m), but the effect of the number of particles are significant with larger particles ($d_p \geq 1.5 \times 10^{-4}$ m), and this dependency is close to a power law, which is shown as a line. Figure 7(b) shows that particle diameter has an increasingly greater impact on the noise generation.

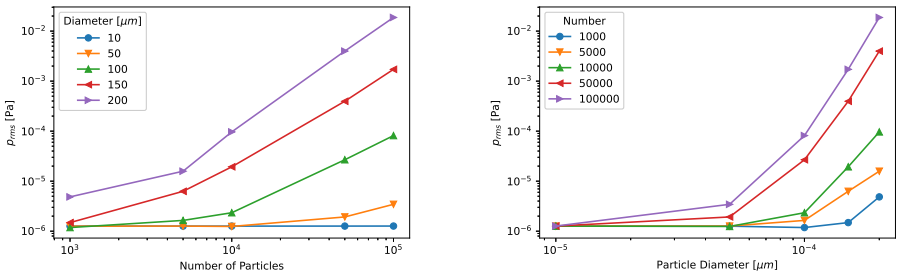

(a) Number of particles (b) Particle diameter

Figure 7: Variation of p_{rms} with increase particle count and diameter relative to $u_0^* = 0.0504$.

Figure 8 shows the same cases as Fig. 7(a), but with $u_0^* = 0.2016$. The largest noise of all cases with $u_{rms} = 0.2016$ is on the order of 10^{-2} Pa (10^5 suspended particles of $d_p = 2 \times 10^{-4}$ m), which is on par with the maximum p_{rms} of Figure 7. This suggests two competing mechanisms contribute to the acoustic pressure in the far-field. One mechanism is related to the initial condition of the fluid phase and is more significant for a small number of particles. The other mechanism is associated with the diameter of particles and is dominant as the particle number increases.

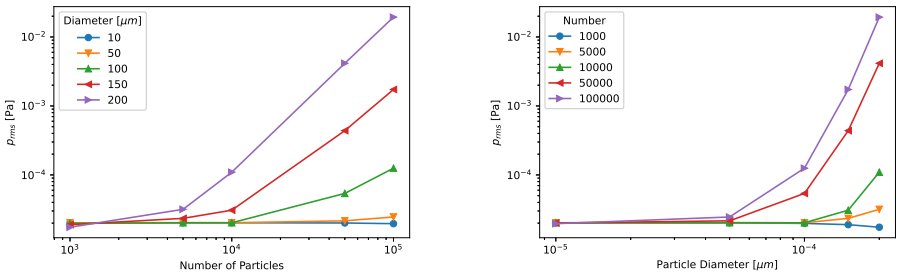

(a) Number of particles (b) Particle diameter

Figure 8: Variation of p_{rms} with increasing particle count and diameter relative to $u_0^* = 0.2016$.

As the effects of particle diameter and number of particles are not independent, we seek to understand their interaction. The volume fraction of the particles, α, calculated as the ratio of the volume of all the particles, $V_p = \sum(1/6)\pi d_p^3$, and the mixture, $V_f = L^3$ for the cubic computational domain, is the most logical choice, since the local disperse-phase volume fraction is shown in the source terms of the C-FW acoustic analogy. Figure 9 shows the change of p_{rms} with respect to the change of volume fraction, and cases of both initial gas velocities are included. In addition, two linear trend lines are fitted for both initial conditions at low particle volume condition. A single trend line is fitted for high volume fraction cases. For volume fraction less than 10^{-6}, the p_{rms} is on the order of 10^{-4} Pa for cases of higher initial velocity $u_{rms} = 0.20$ m/s and 10^{-6} Pa for the cases of $u_{rms} = 0.05$ m/s. Furthermore, the p_{rms} is very weakly dependent on the volume

fraction, and scales as $\alpha^{3/20}$ and $\alpha^{1/100}$, respectively (essentially close to the zeroth power). This implies that the fluid turbulence dominates the noise production mechanism at low volume fraction. On the other hand, the far-field noise depends strongly on the volume fraction when it exceeds 10^{-5}, and the p_{rms} predictions collapse on a single linear trend line. The p_{rms} scales close to the five halves (5/2) power of the volume fraction, which indicates that the noise source is dominated by the disperse phase.

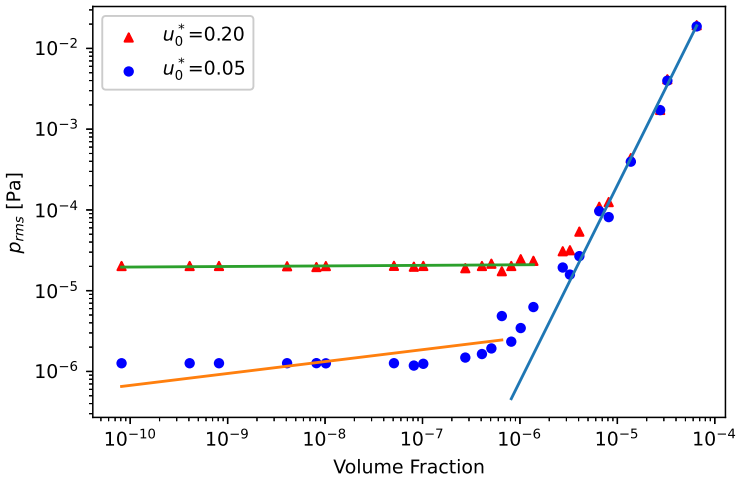

Figure 9: Variation of p_{rms} with respect to particle volume fraction.

This is close to the predicted power of seven-thirds (7/3) given by Crighton and Ffowcs Williams [31] in their scaling analysis of the dipole and quadrupole sources in the limit of a dusty gas. Under the assumption of a dusty gas, where the particles responsively follow the flow, the monopole source and the term of displaced momentum in the dipole sources are negligible. In contrast, the drag force becomes the dominant contributing term in the dipole sources. Moreover, the dipole radiation is equivalent to an amplification of the quadrupole sources when the mass concentration of particles is large. The radiation power scales as the seven thirds (7/3) power of mass concentration, given that the mechanical power of dusty gas and clean gas are same, and scales as the fourth (4) power if the gas characteristic velocities are the same.

We compute the sound pressure associated with monopole, dipole, and quadrupole terms on the right hand side of Eqn. (22). Figures 10 and 11 show the p_{rms} of the portion of the monopole source term, $\frac{\partial Q}{\partial t}$, for the initial velocity u_0^* of 0.0504 and 0.2016 m/s, respectively. We find that the scaling of noise on the total number and diameter of the particles are weakly dependent on each other. This is more apparent when the particle diameters are greater than 10^{-4} m, and the slopes in Figure 11(b) depend on the number of particles. Scaling on both particle diameter and number of particles are not significantly changed with respect to different initial velocities. Noise of monopole sources strongly depend on the volume fraction of the particles, and this source scales

close to the five-halves (5/2) power of volume fraction. The noise from the dipole sources, $-\frac{\partial G_i}{\partial x_i}$ in Eqn. (22), also increases with the increasing number and diameter of particles (as shown in Figures 13 and 14). Figure 15 shows the variation of noise due to the dipole sources with respect to changing volume fraction of particles. The scaling is proportional to the seventeen tenths (17/10) power of the volume fraction. Moreover, the order of magnitude of the noise from monopole and dipole sources are comparable. Both the monopole and dipole sources radiate noise to the far-field and they cannot be neglected.

Figures 16, 17, and 18 show the change of p_{rms} from the quadrupole sources, $\frac{\partial^2 T_{ij}}{\partial x_i \partial x_j}$, with respect to total number, diameter, and volume fraction of particles. The noise radiated from the quadrupole sources is not strongly affected by the number and diameter of the particles, especially in the isotropic turbulent suspension with $u_0^* = 0.2016$ m/s. We observe strong two-way coupling between quadrupole sources and turbulence when the particle diameter becomes greater than 100 µm (see Figure 17(a)). Figure 18 also shows that the quadrupole sources do not depend on volume fraction of particles, but are strongly affected by the difference in the initial velocity. However, the order of magnitude of noise generated by the quadrupole sources is significantly less than the monopole and dipole for volume fraction of particles over 10^{-7}. In other words, the quadrupole sources dominate the noise generation process, when the volume fraction is low, and the particle-laden flow is not very different from single-phase isotropic turbulent flow. However, as the volume fraction increases, the main noise sources become the monopole and dipole sources, and the particles generate the most dominated noise in the far-field.

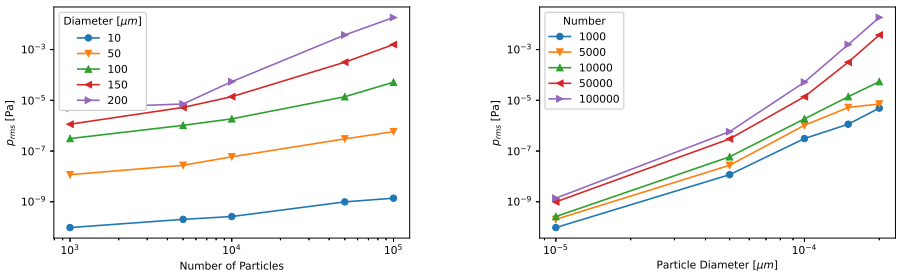

(a) Number of particles

(b) Particle diameter

Figure 10: p_{rms} due to monopole sources with increasing particle number and diameter at $u_0^* = 0.0504$.

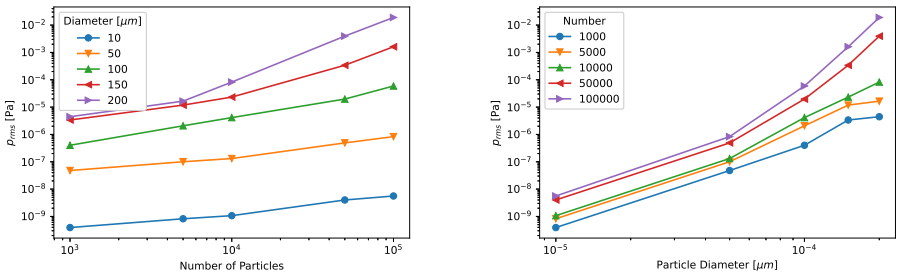

(a) Number of particles (b) Particle diameter

Figure 11: p_{rms} due to monopole sources with increasing particle number and diameter at $u_0^* = 0.2016$.

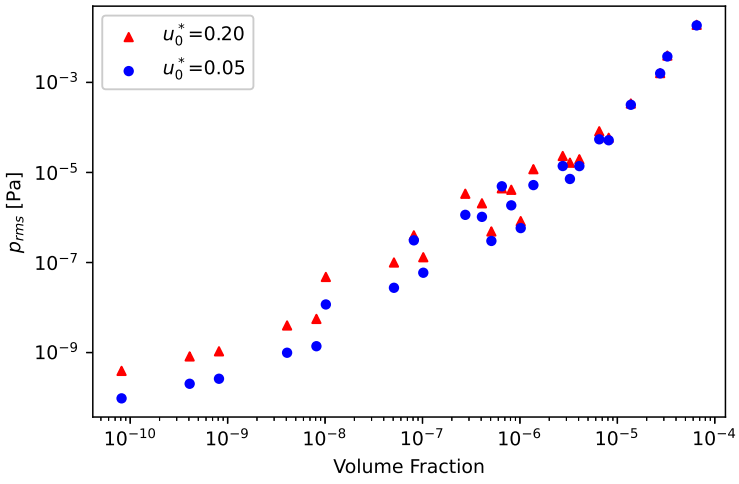

Figure 12: p_{rms} due to monopole sources with increasing particle volume fraction.

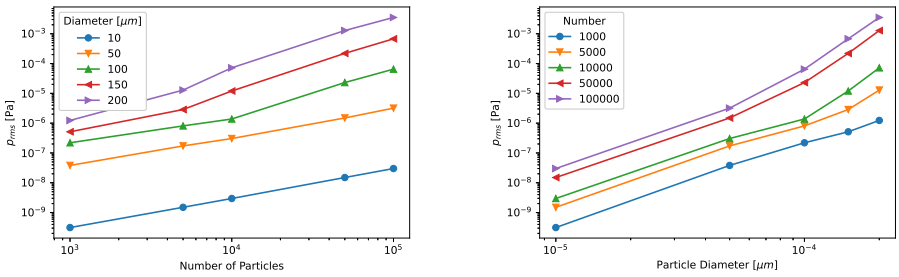

(a) Number of particles (b) Particle diameter

Figure 13: p_{rms} due to dipole sources with increasing particle number and diameter at $u_0^* = 0.0504$.

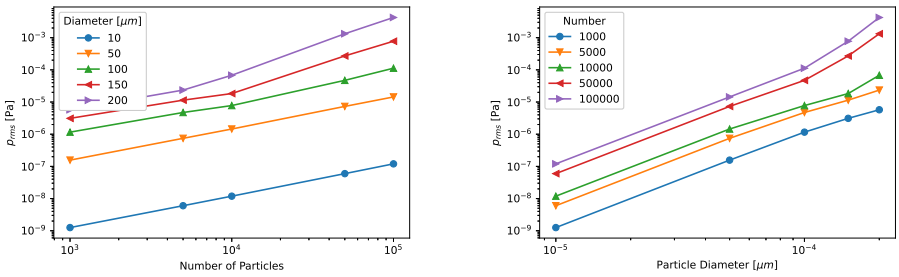

(a) Number of particles (b) Particle diameter

Figure 14: p_{rms} due to dipole sources with increasing particle number and diameter at $u_0^* = 0.2016$.

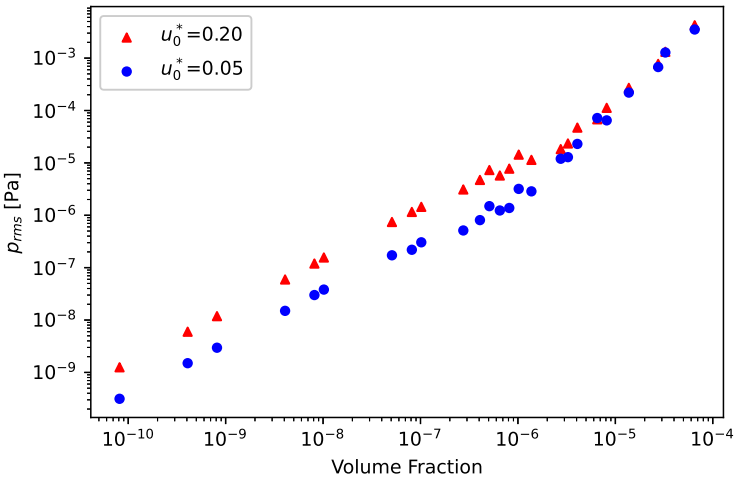

Figure 15: p_{rms} due to dipole sources with increasing particle volume fraction.

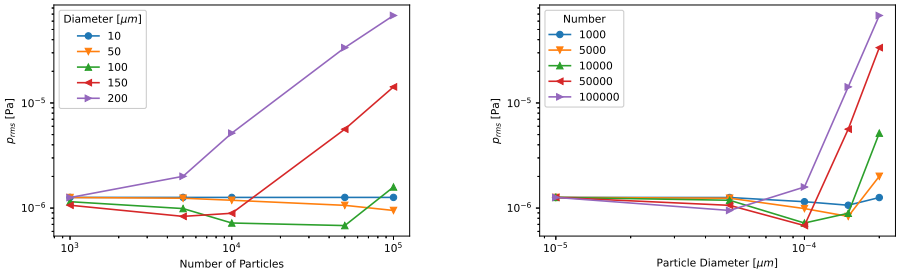

(a) Number of particles

(b) Particle diameter

Figure 16: p_{rms} due to quadrupole sources with increasing particle number and diameter at $u_0^* = 0.0504$.

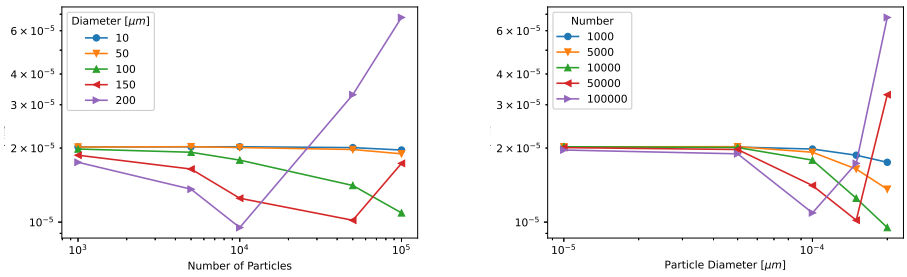

(a) Number of particles (b) Particle diameter

Figure 17: p_{rms} due to quadrupole sources with increasing particle number and diameter at $u_0^* = 0.2016$.

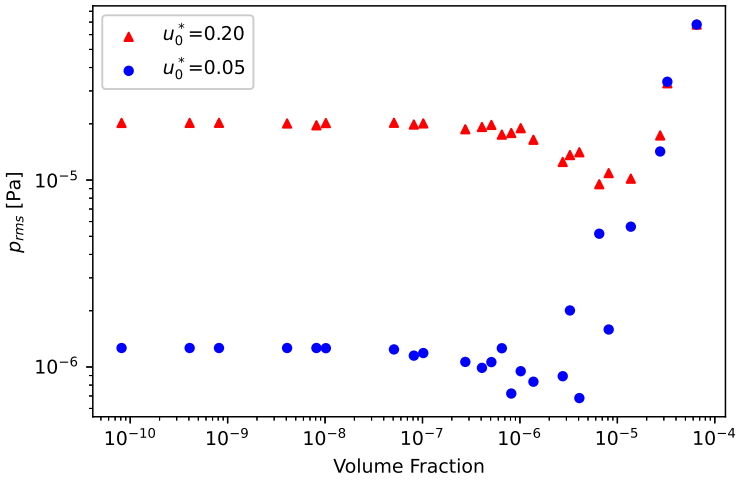

Figure 18: p_{rms} due to quadrupole sources with increasing particle volume fraction.

4. Summary and Conclusion

We performed DNS simulations using an advanced multiphase flow solver to find numerical solutions of the compressible Navier-Stokes equations within a cubic domain that contains up to a hundred thousand particles. Boundary conditions are periodic in all directions. The initial fluid velocity is prescribed using Krianchnan's [34] procedure, which ensures the velocity field is isotropic and divergence-free, and the initial energy is prescribed by Schumann and Patterson [33]. Predictions of acoustic pressure are performed with the C-FW acoustic analogy.

We find that the total number of particles and particle diameters have an interaction effect on the far-field noise. The scaling of rms acoustic pressure with the total number

and diameter of particles depend on each other. Moreover, two competing noise generation mechanisms are observed. The acoustic p_{rms} scales as five-halves (5/2) power with increasing volume fraction for cases with significant number of particles. Here, the monopole and dipole terms dominate the quadrupole term of traditional acoustic analogy theory when a large number of particles with significant diameter are present.

Acknowledgements

This research is supported by the Florida Space Research Initiative (SRI) OR-DRPD-SRI2019: Prediction and Reduction of Noise from Rockets to Eliminate Failure and Fatigue.

References

[1] S. A. McInerny, Rocket noise - a review, in: 13th Aeroacoustics Conference, AIAA, 1990. doi:10.2514/6.1990-3981.
[2] K. Fukuda, S. Tsutsumi, K. Fujii, K. Ui, T. Ishii, H. Oinuma, J. Kazawa, K. Minesugi, Acoustic measurement and prediction of solid rockets in static firing tests, in: 15th AIAA/CEAS Aeroacoustics Conference (30th AIAA Aeroacoustics Conference), 2009, p. 3368.
[3] R. Kenny, C. Hobbs, K. Plotkin, D. Pilkey, Measurement and characterization of space shuttle solid rocket motor plume acoustics, in: 15th AIAA/CEAS Aeroacoustics Conference (30th AIAA Aeroacoustics Conference), 2009, p. 3161.
[4] S. Tsutsumi, K. Fukuda, R. Takaki, E. Shima, K. Fujii, K. Ui, Numerical study on acoustic radiation for designing launch-pad of advanced solid rocket, in: 44th AIAA/ASME/SAE/ASEE Joint Propulsion Conference & Exhibit, 2008, p. 5148.
[5] G. K. Batchelor, The theory of homogeneous turbulence, Cambridge university press, 1953.
[6] J. L. Lumley, G. R. Newman, The return to isotropy of homogeneous turbulence, Journal of Fluid Mechanics 82 (1977) 161–178.
[7] L. Jacquin, O. Leuchter, C. Cambonxs, J. Mathieu, Homogeneous turbulence in the presence of rotation, Journal of Fluid Mechanics 220 (1990) 1–52.
[8] D. Stillinger, K. Helland, C. Van Atta, Experiments on the transition of homogeneous turbulence to internal waves in a stratified fluid, Journal of Fluid Mechanics 131 (1983) 91–122.
[9] F. Jaberi, D. Livescu, C. Madnia, Characteristics of chemically reacting compressible homogeneous turbulence, Physics of Fluids 12 (2000) 1189–1209.
[10] T. K. Patel, S. A. Miller, Source of fine-scale turbulent mixing noise using the navier–stokes equations, AIAA Journal 59 (2021) 2333–2338.
[11] J. Panda, R. Mosher, Microphone phased array to identify liftoff noise sources in model-scale tests, Journal of Spacecraft and Rockets 50 (2013) 1002–1012.
[12] W. Horne, N. Burnside, J. Panda, C. Brodell, Measurements of unsteady pressures near the plume of a solid rocket motor, 15th AIAA/CEAS Aeroacoustics Conference, AIAA Paper 2009-3323 (2009). doi:10.2514/6.2009-3323.
[13] K. D. Squires, J. K. Eaton, Particle response and turbulence modification in isotropic turbulence, Physics of Fluids A: Fluid Dynamics 2 (1990) 1191–1203. URL: https://doi.org/10.1063/1.857620. doi:10.1063/1.857620.
[14] M. Boivin, O. Simonin, K. D. Squires, Direct numerical simulation of turbulence modulation by particles in isotropic turbulence, Journal of Fluid Mechanics 375 (1998) 235–263.
[15] S. Elghobashi, G. C. Truesdell, On the two-way interaction between homogeneous turbulence and dispersed solid particles. i: Turbulence modification, Physics of Fluids A: Fluid Dynamics 5 (1993) 1790–1801. URL: https://doi.org/10.1063/1.858854. doi:10.1063/1.858854.
[16] A. Ferrante, S. Elghobashi, On the physical mechanisms of two-way coupling in particle-laden isotropic turbulence, Physics of Fluids 15 (2003) 315–329. doi:10.1063/1.1532731.
[17] W. Sutherland, LII. the viscosity of gases and molecular force, The London, Edinburgh, and Dublin Philosophical Magazine and Journal of Science 36 (1893) 507–531. doi:10.1080/14786449308620508.
[18] S. Balachandar, J. K. Eaton, Turbulent dispersed multiphase flow, Annual Review of Fluid Mechanics 42 (2010) 111–133. doi:10.1146/annurev.fluid.010908.165243.

[19] A. B. Basset, A treatise on hydrodynamics: with numerous examples, volume 2, Deighton, Bell and Company, 1888.
[20] J. Boussinesq, Sur la resistance qu'oppose un fluide indefini en repos, sans pesanteur, au mouvement varie d'une sphere solide qu'il mouille sur toute sa surface, quand les vitesses restent bien continues et assez faibles pour que leurs carres et produits soient negligiables, CR Acad. Sc. Paris 100 (1885) 935–937.
[21] C. Oseen, Neuere Methoden und Ergebnisse in der Hydrodynamik, 1927.
[22] C. T. Crowe, Multiphase Flow with Droplets and Particles, CRC press, 2012.
[23] Z. Naumann, L. Schiller, A drag coefficient correlation, Z. Ver Deutsch. Ing 77 (1935) 318–323.
[24] W. Ranz, W. R. Marshall, et al., Evaporation from drops, Chemical Engineering Progress 48 (1952) 141–146.
[25] F. Najjar, J. Ferry, A. Haselbacher, S. Balachandar, Simulations of Solid-Propellant Rockets: Effects of Aluminum Droplet Size Distribution, Journal of Spacecraft and Rockets 43 (2006) 1258–1270. doi:10.2514/1.17326.
[26] S. Annamalai, B. Rollin, F. Ouellet, C. Neal, T. L. Jackson, S. Balachandar, Effects of initial perturbations in the early moments of an explosive dispersal of particles, Journal of Fluids Engineering 138 (2016) 070903. doi:10.1115/1.4030954.
[27] A. C. Haselbacher, S. Balachandar, S. Kieffer, Open-ended shock tube flows: Influence of pressure ratio and diaphragm position, AIAA journal 45 (2007) 1917–1929. doi:10.2514/1.23081.
[28] A. Haselbacher, A WENO reconstruction algorithim for unstructured grids based on explicit stencil construction, in: 43rd AIAA Aerospace Sciences Meeting and Exhibit, American Institute of Aeronautics and Astronautics, 2005. URL: https://doi.org/10.2514/6.2005-879. doi:10.2514/6.2005-879.
[29] A. A. Wray, Minimal storage time advancement schemes for spectral methods, NASA Ames Research Center, California, Report No. MS 202 (1990).
[30] A. Haselbacher, F. Najjar, J. Ferry, An efficient and robust particle-localization algorithm for unstructured grids, Journal of Computational Physics 225 (2007) 2198–2213. doi:10.1016/j.jcp.2007.03.018.
[31] D. G. Crighton, J. E. F. Williams, Sound generation by turbulent two-phase flow, Journal of Fluid Mechanics 36 (1969) 585. doi:10.1017/s0022112069001868.
[32] K. S. Brentner, F. Farassat, Modeling aerodynamically generated sound of helicopter rotors, Progress in Aerospace Sciences 39 (2003) 83–120.
[33] U. Schumann, G. S. Patterson, Numerical study of pressure and velocity fluctuations in nearly isotropic turbulence, Journal of Fluid Mechanics 88 (1978) 685–709. doi:10.1017/s0022112078002347.
[34] R. H. Kraichnan, The structure of isotropic turbulence at very high reynolds numbers, Journal of Fluid Mechanics 5 (1959) 497–543.
[35] S. Sarkar, M. Y. Hussaini, Computation of the sound generated by isotropic turbulence, Technical Report, Institute for Computer Applications in Science and Engineering, 1993.
[36] B. Rosa, H. Parishani, O. Ayala, L.-P. Wang, Settling velocity of small inertial particles in homogeneous isotropic turbulence from high-resolution dns, International Journal of Multiphase Flow 83 (2016) 217–231.
[37] N. Mansour, A. Wray, Decay of isotropic turbulence at low reynolds number, Physics of Fluids 6 (1994) 808–814.
[38] P. Burattini, P. Lavoie, A. Agrawal, L. Djenidi, R. Antonia, Power law of decaying homogeneous isotropic turbulence at low reynolds number, Physical Review E 73 (2006) 066304.